



Evaluation of eight nonlinear crystals for phase-matched Terahertz second-order difference-frequency generation at room temperature

Cyril Bernerd, Patricia Segonds, Jérôme Debray, Jean-François Roux, Emilie Héroult, Jean-Louis Coutaz, Ichiro Shoji, Hiroaki Minamide, Hiromasa Ito, Dominique Lupinski, et al.

► To cite this version:

Cyril Bernerd, Patricia Segonds, Jérôme Debray, Jean-François Roux, Emilie Héroult, et al.. Evaluation of eight nonlinear crystals for phase-matched Terahertz second-order difference-frequency generation at room temperature. *Optical Materials Express*, 2020, 10 (2), pp.561. 10.1364/OME.383548 . hal-02450500

HAL Id: hal-02450500

<https://hal.science/hal-02450500>



Submitted on 25 Aug 2023

HAL is a multi-disciplinary open access archive for the deposit and dissemination of scientific research documents, whether they are published or not. The documents may come from teaching and research institutions in France or abroad, or from public or private research centers.

L'archive ouverte pluridisciplinaire **HAL**, est destinée au dépôt et à la diffusion de documents scientifiques de niveau recherche, publiés ou non, émanant des établissements d'enseignement et de recherche français ou étrangers, des laboratoires publics ou privés.



Evaluation of eight nonlinear crystals for phase-matched Terahertz second-order difference-frequency generation at room temperature

CYRIL BERNERD,¹ PATRICIA SEGONDS,¹ JÉRÔME DEBRAY,¹
JEAN-FRANÇOIS ROUX,² EMILIE HÉRAULT,² JEAN-LOUIS COUTAZ,²
ICHIRO SHOJI,³  HIROAKI MINAMIDE,⁴ HIROMASA ITO,⁴
DOMINIQUE LUPINSKI,⁵ KEVIN ZAWILSKI,⁶ PETER
SCHUNEMANN,⁶  XINYUAN ZHANG,⁷ JIYANG WANG,⁷ ZHANGUI
HU,⁷ AND BENOÎT BOULANGER^{1,7,*}

¹Université Grenoble Alpes CNRS, Grenoble INP, Institut Néel, 38000 Grenoble, France

²Laboratoire IMEP-LAHC, Université de Savoie Mont-Blanc, 73376 Le Bourget du Lac Cedex, France

³Department of Electrical, Electronic, and Communication Engineering Chuo University 1-13-27 Kasuga, Bunkyo-ku, Tokyo 112-8551, Japan

⁴Tera-photonics laboratory, RIKEN Center for Advanced Photonics, 519-1399, Aramaki-aoba, Aoba-ku, Sendai, Miyagi 980-0845, Japan

⁵Cristal Laser SA, Parc d'Activités du Breuil - 32, rue Robert Schuman 54850 Messein, France

⁶BAE Systems, MER15-1813, P.O. Box 868, Nashua, NH 03061-0868, USA

⁷Institute of Functional Crystals, Tianjin University of Technology, Tianjin 300384, China

**benoit.boulangier@neel.cnrs.fr*

Abstract: Using terahertz time-domain spectroscopy, we report the principal values of absorption coefficients and refractive indices as a function of wavelength between 0.5 and 2.0 THz of eight attractive nonlinear crystals: YCOB, BNA, LBO, CSP, AGS, CdSe, ZnO and GaP. From these data, we calculated the coherence length and phase-matching conditions associated to the emission of a THz wave from a second-order difference-frequency generation.

© 2020 Optical Society of America under the terms of the [OSA Open Access Publishing Agreement](#)

1. Introduction

The 0.1-10 Terahertz (THz) frequency range has been extensively studied during the last three decades thanks to the introduction of femtosecond lasers and optoelectronic techniques. This frequency domain is very important for both academic research and industrial applications such as control, sensing, imaging and spectroscopy. It already provided potential market developments in numerous areas as defence and security, environment or medicine for example [1–3].

The current commercial THz generators are mainly optically excited antennas [4,5], electronic devices such as HEMT transistors [6] or Schottky diode multipliers [7], and quantum cascade lasers [8]. Nevertheless, the generation of THz waves from a second-order frequency conversion process in dielectric crystals is a competing technique exhibiting several advantages since it can produce high peak-power pulses [9] and open the road towards nonlinear THz photonics [10]; furthermore, the THz pulses can exhibit a very large bandwidth well adapted to perform spectroscopy simultaneously in the THz and MIR ranges [11].

Such a THz generation originates in the Difference-Frequency Generation (DFG) in a nonlinear crystal of two spectral components of the same incoming broadband laser pulse in the visible or infrared range. Another alternative is the DFG between two independent incoming narrowband laser pulses with very close wavelengths, also emitting in the visible or infrared range.

Because the THz frequency is of about 1000 times smaller than the optical one, THz-generation from DFG is often described as Optical Rectification (OR). The magnitude of the optical-to-THz conversion efficiency from DFG is governed by the associated effective second-order nonlinear coefficient in the THz range, and the possibility to achieve phase-matching between the three interacting waves. But the conversion efficiency is limited by the absorption at the THz frequency, mainly due to phonons or to a bad material quality [12,13].

Because DFG is a second-order process, it is then necessary to use non-centrosymmetric nonlinear crystals in order to have non-zero elements of the second-order electric susceptibility tensor. Such conditions of THz generation have been already reported in organic crystals such as DAST [14], DSTMS [15], BNA [16] or OH1 [17], as well as in minerals crystals like KTP [18], PPLN [19], GaAs [20], GaP [21], ZnTe [22], GaSe [23], ZnGeP₂ [24], CdGeP₂ [24], and CdSiP₂ [24]. However, it is often difficult to figure out if THz generation was achieved under phase-matching conditions.

The present paper is devoted to a study of eight attractive crystals in order to identify their ability to generate THz from phase-matched DFG between two incoming narrowband optical beams propagating in the same direction than the generated THz beam, which corresponds to the collinear phase-matching scheme. Like when dealing with nonlinear optics in the visible and infrared ranges, there are many parameters to consider when choosing the good crystal corresponding to a given application in the THz domain: the transparency range, the crystal quality, the size, the linear and nonlinear absorptions, the damage threshold, the angular, spectral and thermal acceptances, the spatial and temporal walk-off attenuations, and the non-linearity. Phase-matching is an issue of particular interest in this area, since it is a key aspect for optimizing the DFG efficiency, which is the main concern of the present article.

Hereafter are listed the chemical formulae and acronyms if any, the crystallographic system and point group, and the optical class of the eight crystals : YCa₄O(BO₃)₃ (YCOB, *monoclinic m*, biaxial) ; N-benzyl-2-methyl-4-nitroaniline (BNA, *orthorhombic mm2*, biaxial); LiB₃O₅ (LBO, *orthorhombic mm2*, biaxial); CdSiP₂ (CSP, *tetragonal 4̄2m*, positive uniaxial); AgGaS₂ (AGS, *tetragonal 4̄2m*, positive uniaxial); CdSe (*hexagonal 6mm*, positive uniaxial); ZnO (*hexagonal 6mm*, positive uniaxial); GaP (*cubic 4̄3m*, isotropic). These eight crystals exhibit very good nonlinear optical properties, including nonlinear and electro-optical coefficients and phase-matching conditions in the visible and infrared ranges, and they can be grown in large size with good optical quality [14–24]. Our objective was then to evaluate their THz transparency range and to determine the principal values of the absorption coefficients and the refractive indices as a function of wavelength in this range. With these data, we aim at calculating how to generate THz from collinear phase-matched DFG, when considering all possible configurations of polarization of the three interacting waves. Such conditions are easy to implement [14–24], even if tilted-pulse-front techniques are very efficient to produce intense THz pulses in crystals exhibiting a strong absorption in the THz domain [25]. All the eight crystals were studied in the same conditions, which ensures the reliability and relevance of their mutual comparison.

Note that we also studied the nonlinear crystals KTiOPO₄ (KTP, *mm2*, biaxial), KTiOAsO₄ (KTA, *mm2*, biaxial), RbTiOPO₄ (RTP, *orthorhombic mm2*, biaxial), La₃Ga_{5.5}Ta_{0.5}O₁₄ (LGT, *trigonal 32*, positive uniaxial), β BaB₂O₄ (BBO, *trigonal 3 m*, positive uniaxial), congruent LiNbO₃ (CLN, *trigonal 3 m*, negative uniaxial), and SiC (*hexagonal 6mm*, positive uniaxial), exactly in the same conditions. But our calculations are not reported here since they did not show any possibility of generation from collinear phase-matched DFG from 0.5 to 2 THz. This does not mean that such conditions are not possible in these crystals for another THz range.

2. Absorption coefficients and refractive indices

We focused on the 0.1–2.0 THz range over which we measured transmission spectra under polarized light by using the Time-Domain Spectroscopy (TDS) method [26,27]. We used

two different experimental set-ups to measure the transfer function of the crystals in the range of interest. For both systems, a pair of LTG-GaAs photoconductive antennas pumped by a 80-fs-duration and 82-MHz-repetition rate Ti:Sapphire laser allows for the coherent emission and detection of the THz pulses. Using a classical quasi-optical set-up including high resistivity Silicon lenses, pairs of parabolic mirrors and possibly Teflon lenses, the THz beam is focused down to 1~2 mm at the sample location. For the first system (*I*) all measurements were performed in a chamber where the relative humidity was kept below 10% thanks to an air-drying device, while for the second system (*II*) the lack of such a device makes the relative humidity larger (50%) along the 1-m-long THz beam path. As a consequence, for this system *II*, the THz signal is disturbed by water vapor absorption. The two set-ups also differ from the acquisition. In system *I*, the time domain signals are recorded in a single scan using a slow optical delay line and the noise level is reduced thanks to the 300-ms-integration time of a lock-in-amplifier. In system *II*, we used a Terahertz Registration System (TRS 16) from Teravil Inc. that consists in a fast scan optical delay line and a dedicated THz receiver and software. In this case, the noise is reduced thanks to the averaging of 1024-scan traces. Both systems give similar performances in term of Signal to Noise Ratio and Dynamics. System *I* was used to characterize LBO, CSP and AGS while system *II* was used for the characterization of CdSe, YCOB, ZNO and GaP. We checked that the use of two different experimental benches did not lead to results discrepancy by characterizing BNA with both systems and comparing the refractive indices and losses obtained with the two different data sets.

For each crystal, we recorded one reference signal (without sample) and the signal transmitted by the sample over a time window of at least 50 ps. Note that the recorded THz spectrum from TDS is ranging from 0.1 up to 5.0 THz. But the useful spectrum is generally limited to 0.3–2.0 THz for the two experimental set-ups because of the weaker dynamics at the lowest and highest frequencies. We checked that the THz signal is linearly polarized with respect to the photoconductive antenna orientation. All measurements were performed at room temperature (22 °C).

Each studied nonlinear crystal was cut as a slab polished to optical quality and stuck on a support while properly oriented according to the polarization of the THz beam. A numerical time-domain windowing of the THz pulse was sometime necessary in order to improve the quality of the recorded data and to reduce the Fabry Perot effect due to the round trip of the pulse inside the crystal. However, in very thin slabs, it was difficult to numerically separate the first temporal echo from the main transmitted THz pulse so that residual oscillations are still observed in the depicted transmission spectra. In any case, the refractive index and the absorption losses of each sample were extracted from the experimental data following the procedure described in Ref. [26].

GaP crystal belonging to the isotropic optical class, transmission spectra can be recorded along any direction of propagation and any orientation of the THz beam linear polarization since there is no birefringence. Then the transmission coefficient $T(\lambda)$ can be determined. In uniaxial crystals, as CSP, AGS, CdSe or ZnO, one slab cut oriented in the dielectric frame (x, y, z) must be used. With a slab cut in any direction of the equatorial plane (x, y) and with the linear polarization of the THz beam successively oriented perpendicular to the z -axis and to the (x, y) plane, the ordinary and extraordinary transmission coefficients, *i.e.* $T_o(\lambda)$ and $T_e(\lambda)$ respectively, were accessible. We used the direction of the (x, y) plane, which corresponds to the angles of spherical coordinates ($\theta = 90^\circ, \varphi = 45^\circ$). The case of the biaxial crystals YCOB, BNA and LBO is more complicated since three principal values of the transmission coefficient must be determined: $T_x(\lambda)$, $T_y(\lambda)$ and $T_z(\lambda)$. Through one slab cut oriented along the x -axis, it is possible to measure $T_y(\lambda)$ and $T_z(\lambda)$ by orienting the linear polarization of the THz beam parallel to the y - and z -axis, respectively; $T_x(\lambda)$ and $T_z(\lambda)$ can be determined using another slab oriented along the y -axis, the polarization of the THz beam being oriented parallel to the x -axis and z -axis respectively.

Thanks to the transmission spectra recorded in polarized light by TDS, it has been possible to determine the principal values of the absorption coefficient and of the refractive index in the 0.3–2 THz range, with a relative accuracy of 10^{-1} and 10^{-3} respectively [28]: they are written α and n for an isotropic crystal; (α_o, α_e) and (n_o, n_e) for a uniaxial crystal; $(\alpha_x, \alpha_y, \alpha_z)$ and (n_x, n_y, n_z) for a biaxial crystal. They are depicted hereafter in Figs. 1–8. The slabs can exhibit a different thickness L . The principal values of the refractive indices as a function of wavelength in the visible-infrared transparency range are also plotted alongside in Figs. 1(b)–8(b) with a relative accuracy of 10^{-3} . We used Sellmeier equations ever published: YCOB [29], BNA [30], LBO [31], CSP [32], AGS [33], CdSe [34], ZnO [35], GaP [36].

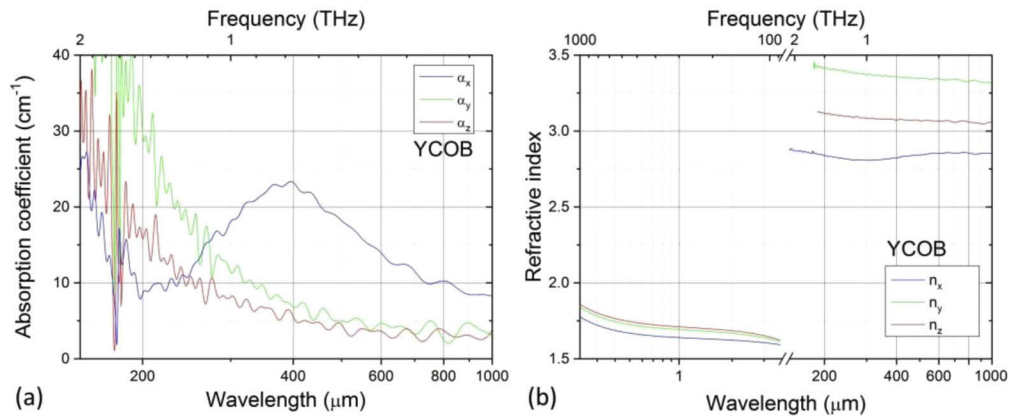


Fig. 1. Principal absorption coefficients and refractive indices of YCOB. The thicknesses are $L = 0.84$ mm along the x -axis and $L = 0.57$ mm along the y -axis. The refractive indices over the visible and infrared ranges are from [29].

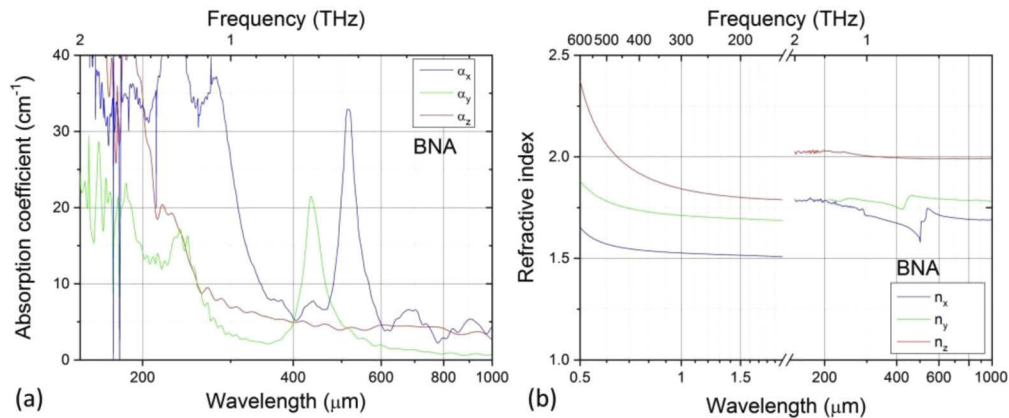


Fig. 2. Principal absorption coefficients and refractive indices of BNA. The thicknesses are $L = 0.86$ mm along the x -axis and $L = 3.00$ mm along the y -axis. The refractive indices over the visible and infrared ranges are from [30].

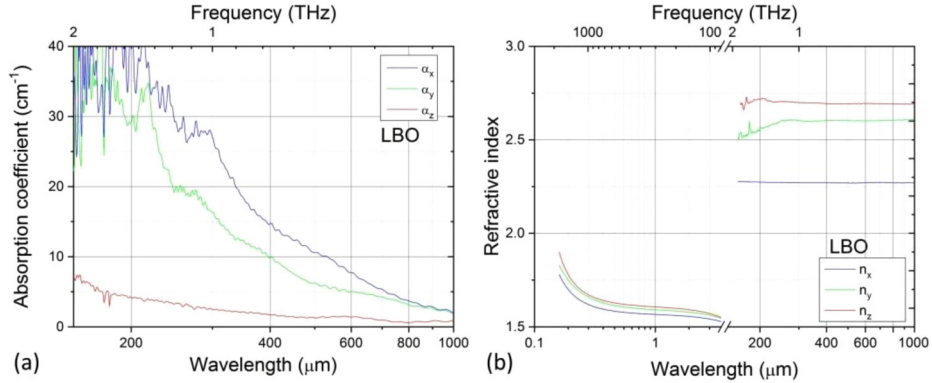


Fig. 3. Principal absorption coefficients and refractive indices of LBO. The thickness is $L = 2.00$ mm along the x -axis and y -axis. The refractive indices over the visible and infrared ranges are from [31].

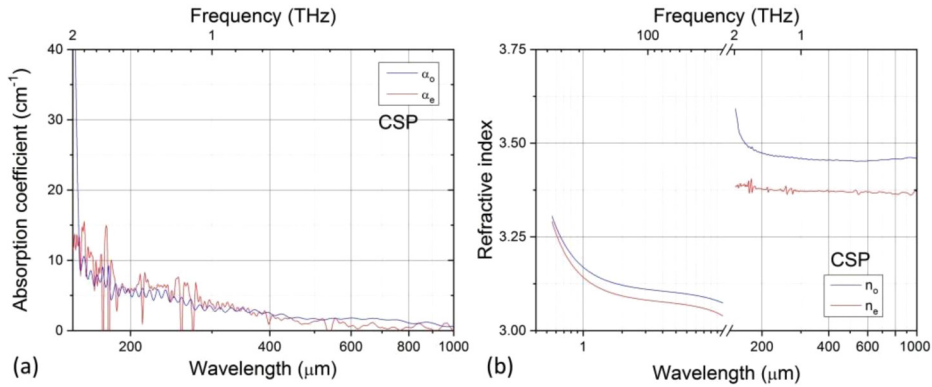


Fig. 4. Principal absorption coefficients and refractive indices of CSP. The thickness is $L = 1.03$ mm along the direction $(\theta = 90^\circ, \varphi = 45^\circ)$. The refractive indices over the visible and infrared ranges are from [32].

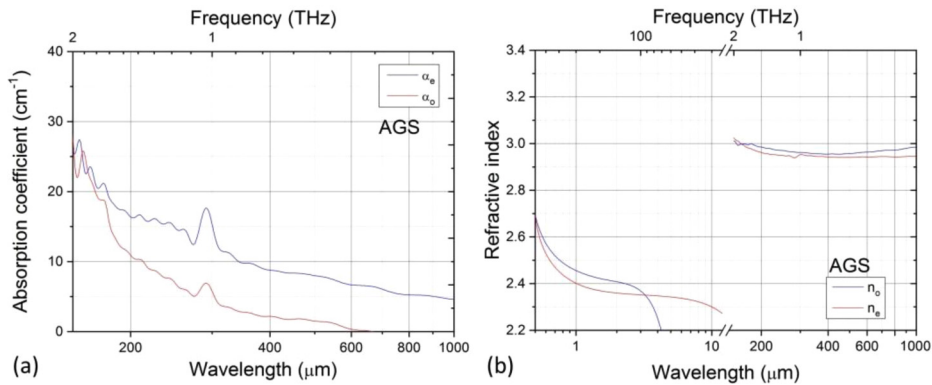


Fig. 5. Principal absorption coefficients and refractive indices of AGS. The thickness is $L = 0.62$ mm along the direction $(\theta = 90^\circ, \varphi = 45^\circ)$. The refractive indices over the visible and infrared ranges are from [33].

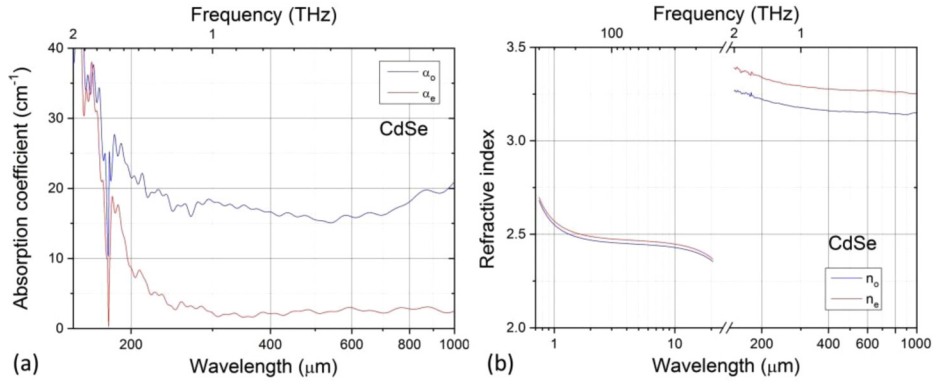


Fig. 6. Principal absorption coefficients and refractive indices of CdSe. The thickness is $L = 0.71$ mm along the direction ($\theta = 90^\circ$, $\varphi = 45^\circ$). The refractive indices over the visible and infrared ranges are from [34].

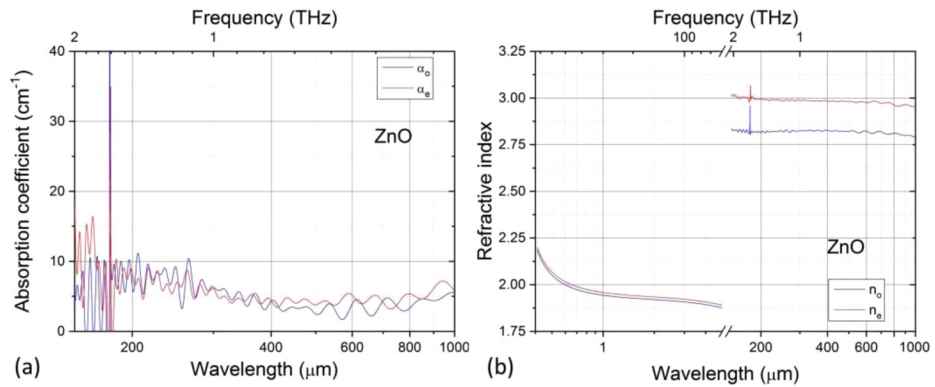


Fig. 7. Principal absorption coefficients and refractive indices of ZnO. The thickness is $L = 0.50$ mm along the direction ($\theta = 90^\circ$, $\varphi = 45^\circ$). The refractive indices over the visible and infrared ranges are from [35].

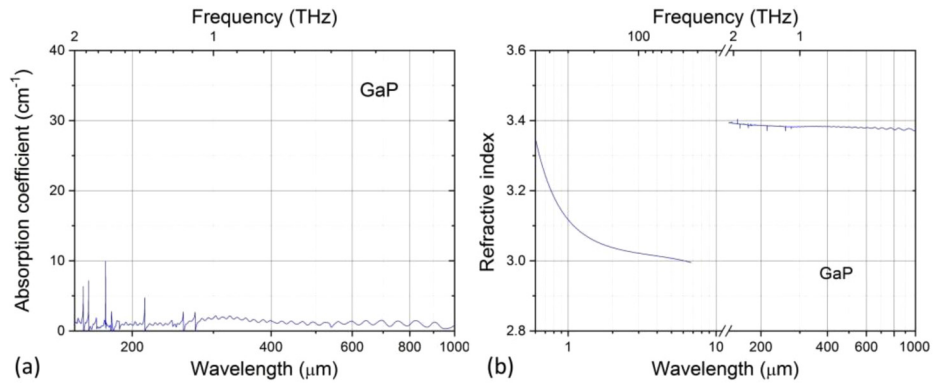


Fig. 8. Absorption coefficient and refractive index of GaP. The thickness is $L = 3.78$ mm along the direction ($\theta = 90^\circ$, $\varphi = 45^\circ$). The refractive indices over the visible and infrared ranges are from [36].

It is not a question here of interpreting the absorption spectra of Figs. 1(a)–8(a). However, we remind that the absorption in mineral and semiconductor crystals is usually increasing above few THz because of transverse-optical phonon resonances in the 5 - 10 THz range or second-order phonon processes at lower frequencies [37]. This is what we clearly observe for YCOB, LBO, CSP, AGS and CdSe. For ZnO and GaP crystals, such a behavior is less pronounced in the studied frequency range because the first phonon lines appear well above 2 THz: at 12.4 THz for ZnO [38] and 11 THz for GaP [39]. On its side, the organic crystal BNA shows more complex absorption resonances because of phonon absorption lines below 1 THz [40]. Discussing the experimental absorption spectra according to losses at the THz wavelengths and to the orientation of the linear polarization of the interacting waves is of prime importance as these properties will have a direct impact onto the possible crystal cut and the dimensions of the THz generator. For instance, the optimal crystal thickness will be both determined by the value of the absorption coefficient and the coherence length [27].

Figs. 4(a) and 7(a) show that according to the absorption coefficient values, the uniaxial crystals CSP and ZnO are quasi isotropic in the 0.5–2.0 THz range. On the contrary, the ratio of the principal absorption coefficients can reach 30% for the other uniaxial or biaxial studied crystals. According to Figs. 1(a)–8(a), the absorption coefficients range between 40 cm^{-1} and 1 cm^{-1} in the 0.3–2.0 THz range. The less absorbing crystal is GaP, with an absorption coefficient below 2 cm^{-1} over the 0.5–2.0 THz range as shown in Fig. 8. A comparison of the other crystals shows that α_z of YCOB, BNA and LBO, (α_o, α_e) of CSP and ZnO, α_e of AGS and CdSe are below 5 cm^{-1} between 0.5 and 1.0 THz; α_z of YCOB and LBO, α_e of CSP, α_o and α_e of AGS and CdSe are below 10 cm^{-1} between 1.0 and 1.5 THz; α_z of LBO, (α_o, α_e) of CSP and ZnO are below 10 cm^{-1} between 1.5 and 2.0 THz. Thus it appears from values of the absorption coefficient shown in Figs. 1(a)–8(a) that CSP, CdSe, ZnO and GaP are globally the most advantageous nonlinear crystals for an emission in the 0.3–2.0 THz range.

Since the visible-infrared transparency range of the eight crystals is always separated from the 0.3–2.0 THz transparency range by large absorption bands [29,36], two different and independent behaviors of the principal refractive indices as a function of wavelength are expected in these two ranges, each of them being governed by two different sets of oscillators. Thus, the principal values of the refractive indices as a function of wavelength that are plotted in Figs. 1(b)–8(b) in the visible-infrared transparency range using the Sellmeier equations from [29–36] cannot be extrapolated for fitting the refractive indices that we determined from TDS in the 0.3–2.0 THz range. The principal refractive indices spectra of Figs. 1(b)–8(b) show that their magnitude is much higher in the 0.3–2.0 THz range than in the visible and near-infrared. One exception is the organic crystal BNA where we even found a correspondence between the values of n_z in the THz range and those of n_x and n_y in the visible-infrared range.

Even if we report very interesting data from TDS for the eight studied crystals, it is difficult at this step to prejudice any possibility of a THz emission from collinear phase-matched DFG, which will be done precisely in the next part by the calculation. Note that the absorption coefficient onto the optical-to-THz conversion efficiency, especially in the THz range, is not taken into account in this paper. The corresponding calculation can be found in Ref. [27].

3. Phase-matching conditions from the study of the coherence length

We are considering hereafter a second-order DFG between two incoming waves λ_2 and λ_3 from the visible-infrared transparency range, generating a wavelength λ_1 in the 0.3–2.0 THz range. With the relation of order $\lambda_1 > \lambda_2 > \lambda_3$ and according to the energy conservation, the three previous wavelengths are linked as follows:

$$\frac{1}{\lambda_1} = \frac{1}{\lambda_3} - \frac{1}{\lambda_2} \quad (1)$$

When assuming the undepleted pump approximation and neglecting the absorption coefficient at λ_1 , λ_2 and λ_3 [27,41], the DFG conversion efficiency normalized to its maximal value, η , can be written in the case of three collinear wave vectors as:

$$\eta \propto \chi_{eff}^2(\theta, \varphi) L^2 \text{sinc}^2(\Delta k L / 2) \quad (2)$$

where $\chi_{eff}^2(\theta, \varphi)$ stands for the square value of the associated effective coefficient, L is the crystal length, and (θ, φ) are the angles of spherical coordinates describing any direction of propagation of the three collinear wave vectors in the nonlinear crystal; Δk is the spatial phase-mismatch defined by:

$$\Delta k = 2\pi \left(\frac{n^\pm(\lambda_3, \theta, \varphi)}{\lambda_3} - \frac{n^\pm(\lambda_2, \theta, \varphi)}{\lambda_2} - \frac{n^\pm(\lambda_1, \theta, \varphi)}{\lambda_1} \right) \quad (3)$$

where n^+ and n^- are the two possible values of the refractive index at each wavelength and in the considered direction of propagation [41].

If $\Delta k \neq 0$, the interference between the nonlinear polarization and the radiated wave at λ_1 is successively constructive and destructive over the crystal length, L : it corresponds to non-phase-matching (NPM) conditions leading to a periodical variation of the NPM DFG conversion efficiency, η_{NPM} , with the crystal length L according to Eq. (2). The spatial half-period of such an oscillation, *i.e.* the coherence length l_c , is expressed as:

$$l_c = \frac{\pi}{\Delta k} \quad (4)$$

According to Eqs. (2) and (4), η_{NPM} behaves as $L^2 \text{sinc}^2(\pi L / 2l_c)$, which means that under NPM conditions ($\Delta k \neq 0$), it reaches a maximal value each time the crystal length L is an odd integer multiple of the coherence length l_c . Since the value of l_c can reach several millimeters when λ_1 is generated in the THz range, against a coherence length of several micrometers with λ_1 in the visible-infrared range, it is possible to achieve a non-negligible value of η_{NPM} over $L = l_c$.

Nevertheless, the phase-matching condition (PM), if possible, is the most advantageous configuration to be targeted. It corresponds to $\Delta k = 0$ and in this case, there is a constructive interference between the nonlinear polarization and the radiated wave at λ_1 over the crystal length, L . According to Eq. (4) under PM conditions, the coherence length has an infinite value, *i.e.* $l_c = \infty$, and then Eq. (2) shows that the PM DFG normalized conversion efficiency η_{PM} behaves as L^2 . Thus, a first advantage of PM conditions is to avoid any oscillation and η_{PM} can reach a maximal value over L . Another advantage of PM conditions can be shown by calculating the ratio $\eta_{NPM}(L)/\eta_{PM}(L)$ at the same generated wavelength λ_1 by using Eqs. (2) and (4). This ratio is plotted in Fig. 9 as a function of L without taking into account the absorption of the generated THz wave. Two different values of l_c , 5 mm and 10 mm, were considered as examples. Figure 9 clearly shows that when $L = l_c$, the NPM DFG normalized conversion efficiency η_{NPM} remains only equal to 40.5% of the PM DFG normalized conversion efficiency η_{PM} independently of the value of the coherence length l_c .

PM conditions are found by solving Eq. (3) when $\Delta k = 0$. Only three combinations of the refractive index in terms of n^- and n^+ at each wavelength are compatible with the wavelength dispersion, *i.e.* $n^{-/+}(\lambda_1) < n^{-/+}(\lambda_2) < n^{-/+}(\lambda_3)$ and $\lambda_1 > \lambda_2 > \lambda_3$. However, in the present case λ_2 and λ_3 lie in the visible-infrared transparency range that is different from the THz range of λ_1 ($> \lambda_2 > \lambda_3$) so that $n^{-/+}(\lambda_2) < n^{-/+}(\lambda_3)$, but these two indices are completely disconnected from $n^{-/+}(\lambda_1)$. Thus, given a direction of propagation, any combination of the three refractive indices involved in Eq. (3) can be *a priori* considered, which gives a number of 2^3 since there are two possible values, n^- and n^+ , for each refractive index. These 8 possible combinations are called types I to VIII and are defined in Table 1. Note that Type V is also labelled type 0, and that types I, II and III are the only ones to be allowed when λ_1 , λ_2 and λ_3 belong to the same transparency domain of the crystal [41].

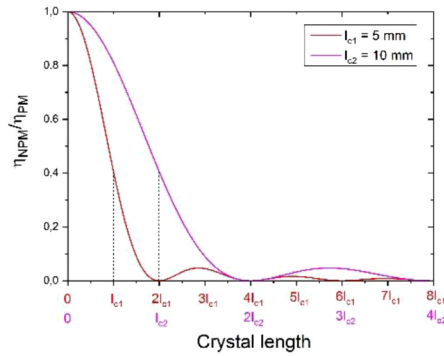


Fig. 9. Calculated ratio between the NPM and PM DFG normalized conversion efficiency, η_{NPM}/η_{PM} as a function of crystal length L for two different values of the coherence length $l_{c1} = 5$ mm and $l_{c2} = 10$ mm, with the absorption of the generated THz wave not taken into account in this comparison.

Table 1. The 8 possible combinations, also labelled as DFG types, in terms of n^- and n^+ of the three refractive indices at the wavelengths λ_1 , λ_2 and λ_3 involved in Eq. (3) in a given direction of propagation.

8 Possible combinations of the refractive indices			Types
λ_1	λ_3	λ_2	
n^+	n^-	n^-	I
n^+	n^-	n^+	II
n^-	n^-	n^+	III
n^-	n^-	n^-	IV
n^+	n^+	n^+	V \equiv 0
n^+	n^+	n^-	VI
n^-	n^+	n^-	VII
n^-	n^+	n^+	VIII

Given a direction of propagation, the study of any of the eight DFG types I to VIII is of interest only if the associated effective coefficient is not nil.

We were able to calculate such conditions for all the selected crystals along the x - and y -axes of the biaxial crystals, and in the (x,y) plane of the uniaxial crystals. These directions are interesting because the corresponding spatial walk-off angle is nil. All these directions and the associated types and effective coefficients calculated from [41] are summarized in Table 2.

We used reliable Sellmeier equations of the eight crystals YCOB, BNA, LBO, CSP, AGS, CdSe, ZnO and GaP for the calculation of the refractive indices at λ_2 and λ_3 in the visible-infrared transparency range [29,36]. Furthermore, we used the direct data shown in Fig. 1(b)–8(b) to determine the value of the refractive index at λ_1 in the 0.3–2.0 THz transparency range; we selected four values of the generated frequency $\nu_1 = c/\lambda_1$ that are well spread out in the 0.3–2.0 THz range: 0.5, 1.0, 1.5 and 2.0 THz. The corresponding values of the principal refractive indices and of the absorption coefficients are shown in Table 2 with an accuracy of 10^{-3} and 10^{-1} , respectively.

In a first step, we calculated the coherence length l_c by using Eqs. (3) and (4), with the data of Tables 1 and 2, as well as the Sellmeier equations from [29,36]. They are plotted in Figs. 10–14 as a function of λ_2 and the corresponding value of λ_3 can be obtained from Eq. (1).

Table 2. Types of DFG and associated DFG effective coefficients χ_{eff} for the 8 selected crystals. Values of the principal absorption coefficients α_i and of the refractive indices n_i at the THz generated wavelength $\lambda_1 = c/\nu_1$; the subscript e stands for “extraordinary”; $\chi_a = -\frac{1}{2}\chi_{zxy} - \frac{1}{2}\chi_{zyx}$

Crystal	Cutting direction	DFG type	χ_{eff}	i	ν_1 (THz)	λ_1 (μm)	$\alpha_i(\lambda_1)$ (cm^{-1})	$n_i(\lambda_1)$
YCOB	x-axis	VII	χ_{yyz}	y	0.5	600	4.6	-
					1	300	11.4	3.371
					1.5	200	29.5	3.417
					2	150	56.0	-
BNA	y-axis	I	χ_{zxx}	z	0.5	600	4.6	1.990
					1	300	6.8	2.005
					1.5	200	34.5	2.028
					2	150	61.2	2.027
BNA	(x, y) plane	V	χ_{zzz}	z	0.5	600	4.6	1.990
					1	300	6.8	2.005
					1.5	200	34.5	2.028
					2	150	61.2	2.027
LBO	x-axis	VII	χ_{yyz}	y	0.5	600	5	-
					1	300	16.3	2.603
					1.5	200	29.1	2.558
					2	150	> 40.0	2.562
CSP	$\theta = 90^\circ \varphi = 45^\circ$	VIII	χ_a	e	0.5	600	0.6	3.369
					1	300	3.7	3.325
					1.5	200	5.7	3.372
					2	150	12.0	3.386
AGS	$\theta = 90^\circ \varphi = 45^\circ$	VIII	χ_a	e	0.5	600	0.5	2.943
					1	300	7.1	2.953
					1.5	200	11.2	2.962
					2	150	25.9	3.025
CdSe	(x, y) plane	V	χ_{zzz}	e	0.5	600	15.9	3.152
					1	300	18.1	3.178
					1.5	200	21.5	3.223
					2	150	38.4	3.266
ZnO	y-axis	I	χ_{zxx}	e	0.5	600	5.1	2.975
					1	300	6.3	2.957
					1.5	200	8.3	2.992
					2	150	18.7	3.009
ZnO	(x, y) plane	V	χ_{zzz}	e	0.5	600	5.1	2.975
					1	300	6.3	2.957
					1.5	200	8.3	2.992
					2	150	18.7	3.009
GaP	$\theta = 90^\circ \varphi = 45^\circ$	II/III	χ_{zxy}	e	0.5	600	1.4	3.380
					1	300	1.8	3.382
					1.5	200	0.8	3.387
					2	150	1.2	3.392

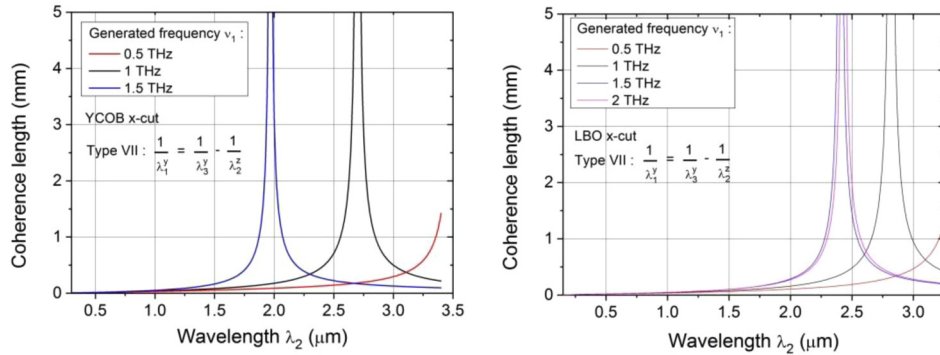


Fig. 10. Calculated coherence length for Type VII DFG in YCOB (a) and Type VII DFG in LBO (b).

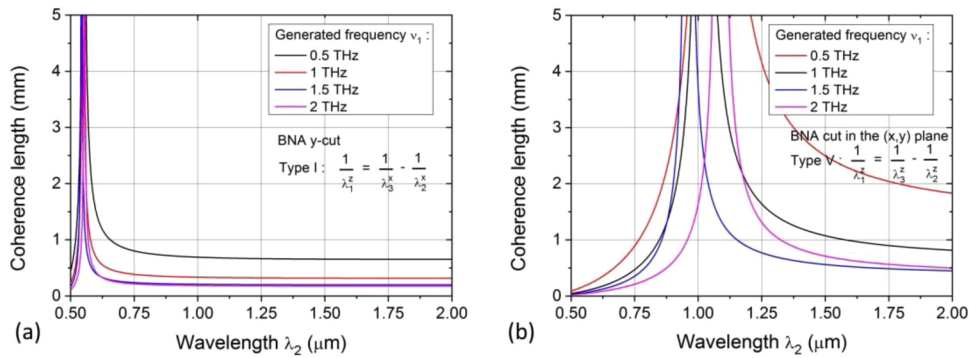


Fig. 11. Calculated coherence length for Type I (a) and Type V (b) DFG in BNA.

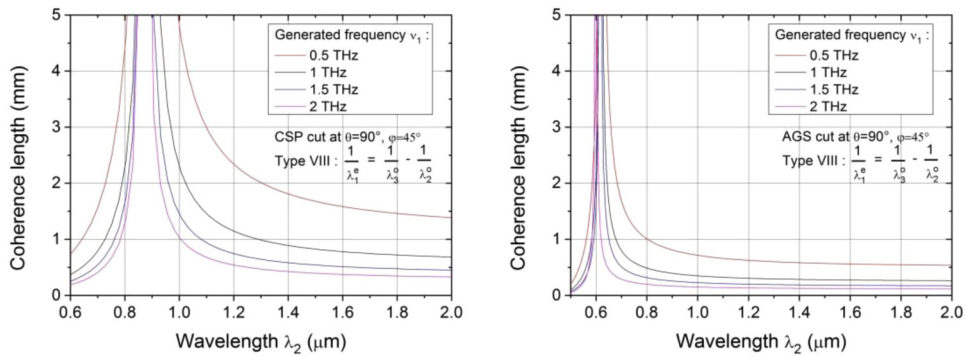


Fig. 12. Calculated coherence length for Type VIII DFG in CSP (a) and Type VIII DFG in AGS (b).

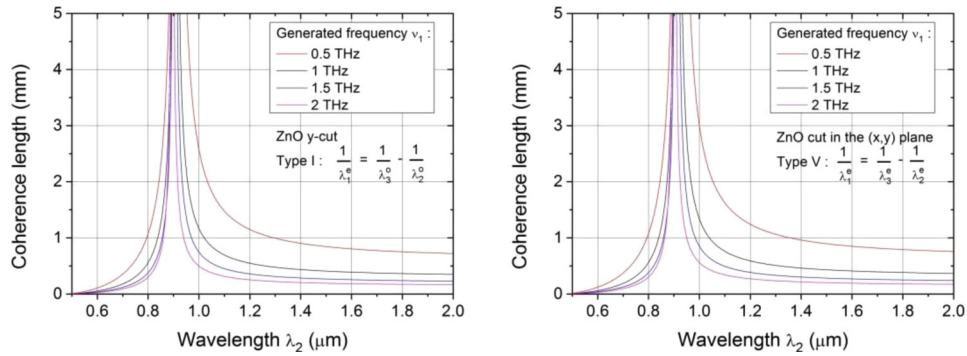


Fig. 13. Calculated coherence length for Type I (a) and Type V (b) DFG in ZnO.

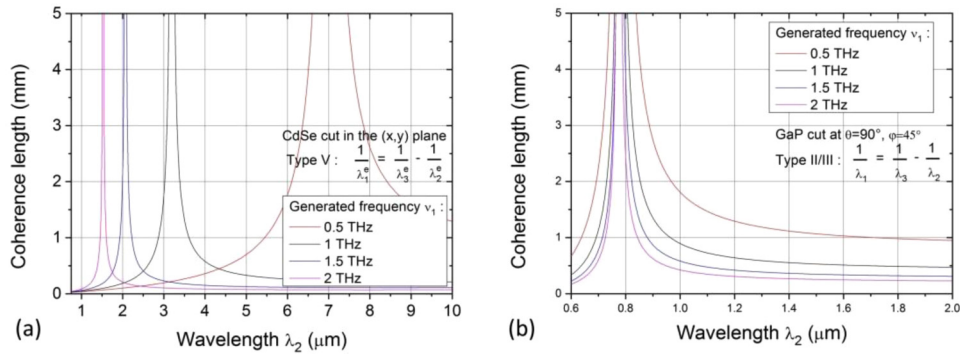


Fig. 14. Calculated coherence length for Type V DFG in CdSe (a) and Type II/III DFG in GaP (b).

In a second step, we were able to determine the PM conditions using the previous curves. Actually, they exhibit a band gap centered at the PM wavelength λ_2^{PM} , which value is thus determined, the corresponding value of λ_3^{PM} being obtained using Eq. (1). These PM wavelengths as well as the corresponding principal refractive indices are summarized in Table 3. The corresponding refractive index at λ_1 is given in Table 2.

On the basis of our calculations, we can assert that phase-matching is possible at the four working frequencies, *i.e.* 0.5 THz, 1.0 THz, 1.5 THz and 2.0 THz, in the eight studied nonlinear crystals excepted in YCOB for which it does not occur at 0.5 THz and 2 THz, and LBO at 0.5 THz.

Note that the calculated phase-matching wavelengths λ_2^{PM} and λ_3^{PM} for GaP, that range around 780 nm (see Fig. 14), are different from those calculated and measured in a previous work where these wavelengths range around 970 and 980 nm for a generation at 2.0 and 1.0 THz, respectively [21]. It is difficult at this step to explain such a strong difference.

At the opposite, our calculations for type V in BNA (Fig. 11) and type VIII in CSP (Fig. 12) well corroborate data previously published in [42] and [24] respectively.

According to the absorption of the generated wave and possible PM achievements, the best crystal is GaP and the total ranking is the following: GaP > CSP > ZnO > AGS > YCOB \approx BNA \approx LBO.

But the comparison between crystals has also to include the incoming phase-matching wavelengths λ_2^{PM} and λ_3^{PM} that have to be not too close to the band gap regarding linear absorption as well as two-photon absorption (TPA).

Table 3. Visible and infrared cut-off wavelengths, phase-matching wavelengths λ_2^{PM} and λ_3^{PM} , and corresponding value of the refractive index $n_{j,k}$ ($j, k = x, y$ or z) for the eight selected crystals. The subscripts o and e stand for “ordinary” and “extraordinary” respectively.

Crystal	Cut- Off (μm)	DFG type	ν_1 (THz)	λ_2^{PM} (μm)	λ_3^{PM} (μm)	j, k	$n_j(\lambda_2^{PM})$	$n_k(\lambda_3^{PM})$
YCOB	0.3	VII	0.5	-	-	-	-	-
			1	2.700	2.676	z, y	1.657	1.643
			1.5	1.960	1.941		1.683	1.667
		3.4		2	-	-	-	-
BNA	0.5	I	0.5	0.5495	0.550		1.596	1.596
			1	0.548	0.547	x, x	1.594	1.598
			1.5	0.542	0.541		1.601	1.603
		2		2	0.554	0.552		1.593
BNA	0.5	V	0.5	1.053	1.051		1.834	1.835
			1	1.018	1.015	z, z	1.840	1.841
			1.5	0.960	0.956		1.850	1.851
		2		2	1.085	1.078		1.831
LBO	0.16	VII	0.5	-	-	-	-	-
			1	2.810	2.784	z, y	1.542	1.542
			1.5	2.400	2.372		1.549	1.549
		3.25		2	2.430	2.391		1.548
CSP	0.6	VIII	0.5	0.880	0.879		3.190	3.190
			1	0.880	0.877	o, o	3.190	3.190
			1.5	0.880	0.876		3.190	3.191
		10		2	0.880	0.875		3.190
AGS	0.5	VIII	0.5	0.620	0.619		2.559	2.559
			1	0.615	0.614	o, o	2.562	2.563
			1.5	0.617	0.615		2.561	2.562
		13.5		2	0.598	0.596		2.574
CdSe	0.75	V	0.5	7.000	6.919		2.459	2.440
			1	3.200	3.166	e, o	2.474	2.454
			1.5	2.060	2.039		2.487	2.468
		25		2	1.520	1.505		2.506
ZnO	0.3	I	0.5	0.913	0.912		1.949	1.949
			1	0.906	0.903	o, o	1.949	1.949
			1.5	0.904	0.900		1.949	1.950
		10		2	0.895	0.890		1.950
ZnO	0.3	V	0.5	0.921	0.920		1.963	1.963
			1	0.914	0.911	e, e	1.964	1.964
			1.5	0.910	0.906		1.964	1.964
		10		2	0.901	0.896		1.965
GaP	0.6	II/III	0.5	0.782	0.781		3.192	3.193
			1	0.782	0.780	-	3.192	3.188
			1.5	0.778	0.775		3.194	3.195
		11		2	0.774	0.770		3.196

The eight previous crystals can be also grouped into three complementary families with respect to the values of λ_2^{PM} and λ_3^{PM} . For BNA, AGS and GaP, the two wavelengths stand in the visible range, *i.e.* respectively around 0.5 μm for BNA (DFG I), and around 0.6 μm and 0.8 μm for AGS and GaP respectively.

It has the advantage that such wavelengths can be obtained thanks to commercial visible pulsed laser sources. However as shown in Table 3, λ_2^{PM} and λ_3^{PM} are too close to the visible cut-off of the visible-infrared transparency ranges so that all the crystals of this first family can exhibit TPA. λ_2^{PM} and λ_3^{PM} stand in the near infrared around 1 μm for the crystals of the second family: 0.9 μm for CSP and ZnO, 1 μm for BNA (DFG V), so that Ti:Sa and Nd:YAG pulsed lasers can be used respectively. The risk of damage induced by TPA is strong in CSP only. The third family includes YCOB, LBO and CdSe when a generation between 1 and 2 THz is targeted. Their incoming phase-matching wavelengths λ_2^{PM} and λ_3^{PM} can be located in the mid-infrared range around 2–3 μm . Then it is the infrared cut-off of the transparency range that can limit the DFG conversion efficiency in YCOB and LBO regarding Table 3. None of the previous problems can occur in CdSe when pumped in the far-infrared around 7 μm for a generation at 0.5 THz but the choice of pulsed laser source is more limited.

Note also that for all the previous crystals, the coherence length is high so that a significant conversion efficiency can be expected even in the NPM condition.

It is impossible at this step to compare all these crystals from the nonlinearity point of view, because all the elements of their second-order electric susceptibility tensor that are involved in the effective coefficient associated to the DFG types shown in Table 2, are only known in their visible or infrared transparency ranges. Since these ranges are governed by different oscillators than those involved in the THz range, it is not possible to use the Miller's rule in order to extrapolate their values in the THz range. A preliminary step would be to consider the value of the electro-optical coefficient as an order of magnitude for the effective coefficient in the THz range, since the THz frequency is close to zero compared to the values of the pump frequencies [43,44]. The eight crystals have electro-optical coefficients close to or larger than those of ZnTe, *i.e.* 4 pm/V around 1 THz [45], which is the reference crystal in the THz range, *e.g.*: 0.97 pm/V for GaP [45], 3.5 pm/V for YCOB [46], 4.5 pm/V for AGS [47], 24 pm/V for BNA [48], and 36 pm/V for LBO [31]. But approximating the second-order nonlinear coefficient to the electro-optical coefficient is only valid far from any THz phonons resonance. The purpose of our future work in this framework will be then to directly measure in the THz range the magnitudes and relative signs of the nonlinear coefficients of the eight studied crystals.

Finally, our study shows that BNA, CSP, AGS, CdSe, ZnO and GaP are tunable from 0.5 up to 2.0 THz, while it is from 1.0 up to 2.0 THz for LBO and from 1.0 up to 1.5 THz for YCOB.

4. Conclusion

We identified YCOB, BNA, LBO, CSP, AGS, CdSe, ZnO and GaP as eight remarkable nonlinear crystals for the generation between 0.5 THz to 2.0 THz using phase-matched difference-frequency-generation. The phase-matching wavelengths as well as the coherence lengths were calculated from absorption and refractive index spectra we measured in the THz range using the TDS technique.

Our calculations show that these eight nonlinear crystals can generate THz light from DFG between two incident wavelengths in the visible or infrared domains that can be provided by commercial optical parametric oscillators (OPO) or generators (OPG).

The theoretical data of phase-matching that we determined provide a unique corpus of information for the design of THz generators, which will make it possible, among other things, to determine the magnitude and relative sign of the nonlinear coefficients of all these crystals in the THz range that is considered here.

It will be also important to perform the same kinds of studies and experiments in other crystals above 2.0 THz, like KTP [49] or 4H-SiC [50] for which phase-matching has been reported in previous works.

Disclosures

The authors declare no conflicts of interest

References

1. Y.-S. Lee, *Principles of Terahertz Science and Technology* (Springer Verlag, 2010).
2. Y.-S. Lee, *Physics and Applications of Terahertz Radiation*, M. Perenzoni and D. J. Paul, eds., Springer Series in Optical Sciences (Springer, 2014).
3. Y.-S. Lee, *Handbook of Terahertz Technologies: Devices and Applications*, H.-J. Song and T. Nagatsuma, eds. (Pan Stanford Publishing, 2015).
4. M. Tani, M. Herrmann, and K. Sakai, "Generation and detection of terahertz pulsed radiation with photoconductive antennas and its application to imaging," *Meas. Sci. Technol.* **13**(11), 1739–1745 (2002).
5. S.-H. Yang, M. R. Hashemi, C. W. Berry, and M. Jarrahi, "7.5% photoconductive emitters with three-dimensional plasmonic contact electrodes," *IEEE Trans. Terahertz Sci. Technol.* **4**(5), 575–581 (2014).
6. A. Lisauskas, A. Rämmer, M. Burakevič, S. Chevtchenko, V. Krozer, W. Heinrich, and H. G. Roskos, "Terahertz emission from biased AlGaIn/GaN high-electron-mobility transistors," *J. Appl. Phys.* **125**(15), 151614 (2019).
7. L. Consolino, S. Bartalini, and P. De Natale, "Terahertz frequency metrology for spectroscopic applications: a review," *J. Infrared, Millimeter, Terahertz Waves* **38**(11), 1289–1315 (2017).
8. M. S. Vitiello, G. Scalari, B. Williams, and P. De Natale, "Quantum cascade lasers: 20 years of challenges," *Opt. Express* **23**(4), 5167–5182 (2015).
9. J. A. Fülöp, L. Pálfalvi, S. Klingebiel, G. Almási, F. Krausz, S. Karsch, and J. Hebling, "Generation of sub-mJ terahertz pulses by optical rectification," *Opt. Lett.* **37**(4), 557–559 (2012).
10. H. A. Hafez, X. Chai, A. Ibrahim, S. Mondal, D. Férachou, X. Ropagnol, and T. Ozaki, "Intense terahertz radiation and their applications," *J. Optics* **18**(9), 093004 (2016).
11. C. Somma, G. Fopini, J. Gupta, K. Reimann, M. Woerner, and T. Elsaesser, "Ultra-broadband terahertz pulses generated in the organic crystal DSTMS," *Opt. Lett.* **40**(14), 3404–3407 (2015).
12. A. Schneider, M. Neis, M. Stillhart, B. Ruiz, R. U. Khan, and P. Günter, "Generation of terahertz pulses through optical rectification in organic DAST crystals: theory and experiment," *J. Opt. Soc. Am. B* **23**(9), 1822–1835 (2006).
13. K. Ravi, W. R. Huang, S. Carbajo, E. A. Nanni, D. N. Schimpf, E. P. Ippen, and F. X. Kärtner, "Theory of terahertz generation by optical rectification using tilted-pulse-fronts," *Opt. Express* **23**(4), 5253–5276 (2015).
14. K. Suizu, K. Miyamoto, T. Yamashita, and H. Ito, "High-power terahertz-wave generation using DAST crystal and detection using mid-infrared powermeter," *Opt. Lett.* **32**(19), 2885–2887 (2007).
15. P. Liu, D. Xu, Y. Li, X. Zhang, Y. Wang, J. Yao, and Y. Wu, "Widely tunable and monochromatic terahertz difference frequency generation with organic crystal DSTMS," *Eur. Phys. Lett.* **106**(6), 60001 (2014).
16. K. Miyamoto, H. Minamide, M. Fujiwara, H. Hashimoto, and H. Ito, "Widely tunable terahertz-wave generation using an N-benzyl-2-methyl-4-nitroaniline crystal," *Opt. Lett.* **33**(3), 252–254 (2008).
17. P. Liu, X. Zhang, C. Yan, D. Xu, Y. Li, W. Shi, G. Zhang, X. Zhang, J. Yao, and Y. Wu, "Widely tunable and monochromatic terahertz difference frequency generation with organic crystal 2-(3-(4-hydroxystyryl)-5,5-dimethylcyclohex-2-enylidene) malononitrile," *Appl. Phys. Lett.* **108**(1), 011104 (2016).
18. M.-H. Wu, Y.-C. Chiu, T.-D. Wang, G. Zhao, A. Zukauskas, F. Laurell, and Y.-C. Huang, "Terahertz parametric generation and amplification from potassium titanyl phosphate in comparison with lithium niobate and lithium tantalite," *Opt. Express* **24**(23), 25964–25973 (2016).
19. C. Zhang, Y. Avetisyan, A. Glosser, I. Kawayama, H. Murakami, and M. Tonouchi, "Bandwidth tunable THz wave generation in large-area periodically poled lithium niobate," *Opt. Express* **20**(8), 8784–8790 (2012).
20. J. E. Schaar, K. L. Vodopyanov, and M. M. Fejer, "Intracavity terahertz-wave generation in a synchronously pumped optical parametric oscillator using quasi-phasematched GaAs," *Opt. Lett.* **32**(10), 1284–1286 (2007).
21. T. Taniuchi and H. Nakanishi, "Collinear phase-matched terahertz-wave generation in GaP crystal using a dual-wavelength optical parametric oscillator," *J. Appl. Phys.* **95**(12), 7588–7591 (2004).
22. F. Blanchard, L. Razzari, H.-C. Banduler, G. Sharma, R. Morandotti, J.-C. Kieffer, T. Ozaki, M. Reid, H. F. Tiedje, H. K. Haugen, and F. A. Hegmann, "Generation of 1.5 μJ single-cycle terahertz pulses by optical rectification from a large aperture ZnTe crystal," *Opt. Express* **15**(20), 13212–13220 (2007).
23. J. Mei, K. Zhong, M. Wang, Y. Liu, D. Xu, W. Shi, Y. Wang, J. Yao, R. A. Norwood, and N. Peyghambarian, "Widely-tunable high-repetition rate terahertz generation in GaSe with a compact dual-wavelength KTP OPO around 2 μm ," *Opt. Express* **24**(20), 23368–23375 (2016).
24. H. P. Piyathilaka, R. Sooriyagoda, V. Dewasurendra, M. B. Johnson, K. T. Zawilski, P. G. Schunemann, and A. D. Bristow, "Terahertz generation by optical rectification in chalcopyrite crystals ZnGeP₂, CdGeP₂ and CdSiP₂," *Opt. Express* **27**(12), 16958–16965 (2019).

25. J. Hebling, G. Almási, I. Kozma, and J. Kuhl, "Velocity matching by pulse front tilting for large-area THz-pulse generation," *Opt. Express* **10**(21), 1161–1166 (2002).
26. L. DuVillaret, F. Garet, and J.-L. Coutaz, "A reliable method for extraction of material parameters in terahertz Time-Domain Spectroscopy," *IEEE J. Sel. Top. Quantum Electron.* **2**(3), 739–746 (1996).
27. J.-L. Coutaz, F. Garet, and V. P. Wallace, *Principles of TeraHertz Time-Domain Spectroscopy* (Pan Stanford Publishing, 2018).
28. L. DuVillaret, F. Garet, and J.-L. Coutaz, "Influence of noise on the characterization of materials by terahertz time-domain spectroscopy," *J. Opt. Soc. Am. B* **17**(3), 452–461 (2000).
29. P. Segonds, B. Boulanger, B. Ménaert, J. Zaccaro, J.-P. Salvestrini, M. D. Fontana, R. Moncorgé, F. Porée, G. Gadret, J. Mangin, A. Brenier, G. Boulon, G. Aka, and D. Pelenc, "Optical characterizations of $\text{YCa}_4\text{O}(\text{BO}_3)_3$ and $\text{Nd:YCa}_4\text{O}(\text{BO}_3)_3$ crystals," *Opt. Mater.* **29**(8), 975–982 (2007).
30. C. Bernerd, P. Segonds, J. Debray, T. Notake, M. Koyama, H. Minamide, H. Ito, and B. Boulanger, "Quadratic nonlinear optical properties of the organic N-benzyl-2-methyl-4-nitroaniline (BNA) biaxial crystal," *Opt. Lett.* **43**(8), 1818–1821 (2018).
31. C. Chen, Y. Wu, A. Jiang, B. Wu, G. You, R. Li, and S. Lin, "New nonlinear optical crystal: LiB_3O_5 ," *J. Opt. Soc. Am. B* **6**(4), 616–621 (1989).
32. V. Kemlin, P. Brand, B. Boulanger, P. Segonds, P. G. Schunemann, K. T. Zawilski, B. Ménaert, and J. Debray, "Phase-matching properties and refined Sellmeier equations of the new nonlinear infrared crystal CdSiP_2 ," *Opt. Lett.* **36**(10), 1800–1802 (2011).
33. A. Harasaki and K. Kato, "New data on the nonlinear optical constant, phase-matching and optical damage of AgGaS_2 ," *Jpn. J. Appl. Phys.* **36**(Part 1, No. 2), 700–703 (1997).
34. G. C. Bhar, "Refractive index interpolation in phase-matching," *Appl. Opt.* **15**(2), 305–307 (1976).
35. *Handbook of Optics*, 3rd Edition, Vol. 4 (McGraw-Hill, 2009).
36. A. S. Barker, "Dielectric dispersion and phonon line shape in gallium phosphide," *Phys. Rev.* **165**(3), 917–922 (1968).
37. M. Schall, H. Helm, and S. R. Keiding, "Far Infrared Properties of Electro-Optic Crystals Measured by THz Time-Domain Spectroscopy," *Int. J. Infrared Millimeter Waves* **20**(4), 595–604 (1999).
38. J. Han, W. Zhang, W. Chen, S. Ray, J. Zhang, M. He, A. K. Azad, and Z. Zhu, "Terahertz Dielectric Properties and Low-Frequency Phonon Resonances of ZnO Nanostructures," *J. Phys. Chem. C* **111**(35), 13000–13006 (2007).
39. A. Leitenstorfer, S. Hunsche, J. Shah, M. C. Nuss, and W. H. Knox, "Detectors and sources for ultrabroadband electro-optic sampling: Experiment and theory," *Appl. Phys. Lett.* **74**(11), 1516–1518 (1999).
40. K. Kuroyanagi, M. Fujiwara, H. Hashimoto, H. Takahashi, S. Aoshima, and Y. Tsuchiya, "Determination of Refractive Indices and Absorption Coefficients of Highly Purified N-Benzyl-2-methyl-4-nitroaniline Crystal in Terahertz Frequency Regime," *Jpn. J. Appl. Phys.* **45**(29), L761–L764 (2006).
41. B. Boulanger and J. Zyss, "Nonlinear optical properties," *Int. Tables Crystallogr. D*, chapter 1.7, 178–219 (2006).
42. T. Notake, K. Nawata, H. Kawamata, T. Matsukawa, F. Qi, and H. Minamide, "Development of an ultra-widely tunable DFG-THz source with switching between organic nonlinear crystals pumped with a dual-wavelength BBO optical parametric oscillator," *Opt. Express* **20**(23), 25850–25857 (2012).
43. G. D. Boyd, T. J. Bridges, M. A. Pollack, and E. H. Turner, "Microwave Nonlinear Susceptibilities Due to Electronic and Ionic Anharmonicities in Acentric Crystals," *Phys. Rev. Lett.* **26**(7), 387–390 (1971).
44. Q. Wu and X.-C. Zhang, "Ultrafast electro-optic field sensors," *Appl. Phys. Lett.* **68**(12), 1604–1606 (1996).
45. A. Yariv, *Quantum Electronics*, 3rd ed. (John Wiley and Sons, 1988).
46. M. Abarkan, J.-P. Salvestrini, D. Pelenc, and M. D. Fontana, "Electro-optic, thermo-optic, and dielectric properties of YCOB and Nd:YCOB crystals: comparative study," *J. Opt. Soc. Am. B* **22**(2), 398–406 (2005).
47. H. Horinaka, H. Sonomura, and T. Miyauchi, "Linear Electro-Optic Effect of AgGaSe_2 ," *Jpn. J. Appl. Phys.* **21**(Part 1, No. 10), 1485–1488 (1982).
48. H. Hashimoto, H. Takahashi, T. Yamada, K. Kuroyanagi, and T. Kobayashi, "Characteristics of the terahertz radiation from single crystals of N-substituted 2-methyl-4-nitroaniline," *J. Phys.: Condens. Matter* **13**(23), L529–L537 (2001).
49. C. R. Wang, Q. K. Pan, F. Chen, G. Lanskie, N. Nikolaev, A. Mamrashev, Y. Andreev, and A. Meshalkin, "Phase-matching in KTP crystal for THz wave generation at room temperature and 81 K," *Infrared Phys. Technol.* **97**, 1–5 (2019).
50. M. P. Fisher, J. Bühler, G. Fitzky, T. Kurihara, S. Eggert, A. Leitenstorfer, and D. Brida, "Coherent field transients below 15 THz from phase-matched difference frequency generation in 4H-SiC," *Opt. Lett.* **42**(14), 2687–2690 (2017).